

Impedance Spectra of the Hydrogen Evolution Reaction at Low Cathodic Overpotentials

Višnja Horvat-Radošević* and Krešimir Kvastek

Centre for Marine and Environmental Research, Ruđer Bošković Institute, P. O. Box 180, HR-10002 Zagreb, Croatia

RECEIVED JULY 29, 2002; REVISED APRIL 9, 2003; ACCEPTED JUNE 16, 2003

Impedance spectra of the hydrogen evolution reaction, HER, at low cathodic overpotentials were analyzed on the basis of the theoretical admittance/frequency function, initially derived for the Volmer-Heyrovsky-Tafel reaction mechanism involving the hydrogen insertion (adsorption + diffusion) step. General principles of the impedance spectroscopy for HER are discussed using schematically constructed impedance spectra. In order to characterize the influence of each impedance parameter on the shape of the spectrum, some simulations of impedance spectra were performed with different values of impedance parameters. Comparative impedance measurements were carried out on deposited rhodium and ruthenium electrodes at -0.040 V vs. r.h.e. in $0.5 \text{ mol dm}^{-3} \text{ H}_2\text{SO}_4$. Impedance parameter values were estimated by curve fitting between theoretical and experimental impedance spectra. In addition to the electron transfer, formation of adsorbed hydrogen and H_2 desorption step, participation of a bulk diffusion step of hydrogen was observed for both electrodes at the lowest frequencies. Comparison between impedance parameter values of the two electrodes suggested faster kinetics of HER at the rhodium electrode.

Key words

impedance spectra
hydrogen evolution reaction
ruthenium electrode
rhodium electrode

INTRODUCTION

The electrochemical impedance technique, EIS, has been often used in investigations of the kinetics of the hydrogen evolution reaction, HER, at various crystalline and amorphous forms of metal and metal alloy substrates and from various electrolyte solutions, producing impedance spectra with one or two relaxation frequencies.^{1–21} In the majority of these investigations, impedance data analysis was based on an already known model structure, owing primarily to Harrington and Conway's postulation of the net rates of individual reactions for the Volmer-Heyrovsky-Tafel mechanism of HER, definition of the surface fraction of adsorbed hydrogen as a potential dependent state variable, and evaluation of the corre-

sponding faradaic and total electrode admittance/frequency functions.²² Thus, impedance spectra measured at higher cathodic overpotentials were commonly analyzed in terms of the potential independent double-layer charging/discharging and potential dependent rate of the electron transfer reaction,^{1–4,6,7,9,11–13,16,19,20} with an additional account for the effect of electrode surface roughness^{2–4,6,7,9,12,20} and sometimes for porosity.^{9,16,19} Special advantage of the technique, however, was seen at lower cathodic overpotentials, where two relaxation frequencies in impedance spectra allowed separation between two capacitive responses.^{1,5,11,12,18,21} In other words, use of the EIS technique made it possible to separate the effects of potential changes of the surface fraction of adsorbed

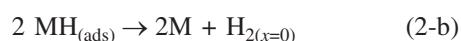
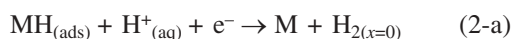
* Author to whom correspondence should be addressed. (E-mail: vhorvat@rudjer.irb.hr)

hydrogen from double-layer effects. On some metals, however, such as palladium,^{10,14,15} platinum,^{1,18} rhodium,²¹ or amorphous iron based alloy,⁴ impedance spectra measured at low overpotentials of HER were not in accord with the predicted shapes, indicating problems in the theoretical impedance model. Explanations of these deviations were mainly focused on some additional process/es such as diffusion of molecular hydrogen toward the bulk of the electrolyte,^{1,18} or hydrogen insertion (absorption + diffusion) within a metal layer.^{4,10,14,15} To account for the deviations observed for the Rh/H₂SO₄ electrode, we have recently derived the general expression for the faradaic admittance/frequency function where faradaic current depends not only on the potential and surface fraction of adsorbed hydrogen, but also on the surface concentration of some diffusing species.²¹ The aim of the present paper is to discuss the possible shapes of faradaic and total impedance spectra that are based on this general faradaic admittance/frequency relationship, and also to compare simulated impedance spectra with those experimentally measured at rhodium and ruthenium/H₂SO₄ electrodes in the region of low cathodic overpotentials of HER.

THEORETICAL ASPECTS OF IMPEDANCE SPECTRA OF HER

Faradic Impedance Modeling of HER

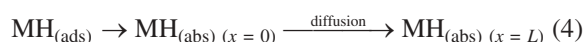
Starting from the well known Volmer-Heyrovsky-Tafel mechanism of HER on metal electrodes, M, in acid solutions^{23–25}



and postulating additional steps as either diffusion of H₂ from the electrode surface at ($x = 0$) toward the bulk of the electrolyte at ($x = b$),^{1,18}



or hydrogen absorption and diffusion of adsorbed hydrogen from the electrode surface at ($x = 0$) through the metal layer of thickness L ,^{10,13–15,24,26}



previously²¹ we derived the general faradaic admittance/angular frequency, ω , function, $Y_f(\omega)$, in the following form:

$$Y_f(\omega) = a_1 + (a_2 b_1 Q + a_2 b_3 d_1 + a_3 d_1 P + a_3 b_1 d_2) (PQ - b_3 d_2)^{-1} \quad (5\text{-a})$$

$$P = q i \omega - b_2 \quad (5\text{-b})$$

$$Q = F M(\omega) - d_3 \quad (5\text{-c})$$

In Eq. (5), $M(\omega)$, q and F are the diffusion flux/concentration transfer function at $x = 0$, charge density necessary for formation of monolayer coverage by adsorbed hydrogen and Faraday constant, respectively. Other parameters are defined as partial derivatives of net production rates of electron transfer, r_e , adsorbed hydrogen, r_θ , and molecular or adsorbed hydrogen, r_c , with respect to the potential, E , fractional surface coverage by adsorbed hydrogen, θ , and surface concentration of hydrogen, c_o :

$$a_1 = -F (\partial r_e / \partial E)_{\theta, c} \quad (6\text{-a})$$

$$a_2 = -F (\partial r_e / \partial \theta)_{E, c} \quad (6\text{-b})$$

$$a_3 = -F (\partial r_e / \partial c_o)_{E, \theta} \quad (6\text{-c})$$

$$b_1 = F (\partial r_\theta / \partial E)_{\theta, c} \quad (6\text{-d})$$

$$b_2 = F (\partial r_\theta / \partial \theta)_{E, c} \quad (6\text{-e})$$

$$b_3 = F (\partial r_\theta / \partial c_o)_{E, \theta} \quad (6\text{-f})$$

$$d_1 = F (\partial r_c / \partial E)_{\theta, c} \quad (6\text{-g})$$

$$d_2 = F (\partial r_c / \partial \theta)_{E, c} \quad (6\text{-h})$$

$$d_3 = F (\partial r_c / \partial c_o)_{E, \theta} \quad (6\text{-i})$$

Under the usual assumptions of independence of r_e on $c_{(x=0)}$, and r_c on E ,^{10,14,15,18,21} $a_3 = 0$ and $d_1 = 0$, so Eq. (5) is reduced to:

$$Y_f(\omega) = a_1 + a_2 b_1 (q i \omega - b_2 - b_3 d_2 Q^{-1})^{-1} \quad (7)$$

If there is no diffusion, or when HER proceeds only by reactions (1) and (2), a_3 , b_3 , d_1 , d_2 , $d_3 = 0$, so Eq. (7) becomes further reduced to:

$$Y_f(\omega) = a_1 + a_2 b_1 (q i \omega - b_2)^{-1} \quad (8)$$

Eq. (8) derived from the general faradaic admittance/frequency Eq. (5), although in different notation, is equivalent to Harrington and Conway's relation postulated for the HER proceeding without diffusion complication.²² Eq. (8) is also equal to the theoretical relation for the electrode admittance that was principally postulated for any irreversible electrode reaction with one state variable besides the potential.^{27,28}

In simple terms of equivalent electrical circuits,^{29,30} Eq. (8) can be rewritten as

$$Z_f(\omega) = (R_1) + [i\omega C_{\text{ad}} + (Z_{\text{rest}})^{-1}]^{-1} \quad (9)$$

with the following definitions of the electrical equivalent circuit elements:

$$C_{ad} = -q a_1^2 (a_2 b_1)^{-1} \quad (10-a)$$

$$R_1 = a_1^{-1} \quad (10-b)$$

$$Z_{rest} = a_2 b_1 (a_1^2 b_2 - a_1 a_2 b_1 + a_1^2 b_3 d_2 Q^{-1})^{-1} \quad (10-c)$$

Z_{rest} defined by Eq. (10-c) is the impedance parallel to capacitive impedance $(i\omega C_{ad})^{-1}$, and depends on the specific reaction mechanism.²¹ It can be shown that for the specific mechanism described by reactions (1) and (2), Z_{rest} is pure resistance R_2 related to the combination of partial derivatives of reaction rates with respect to E and θ .²¹ For the mechanism described by Eqs. (1), (2) and (4), however, Z_{rest} is a parallel sum of resistance R_2 and impedance $(R_3 + Z_d)$, where R_2 is defined as in,²² while R_3 and Z_d are different combinations of partial derivatives of reaction rates with respect to E , θ and $c_{(x=0)}$.²¹ In these two cases, Eq. (9) takes following specific forms:

$$Z_f(\omega) = R_1 + [i\omega C_{ad} + (R_2)^{-1}]^{-1} \quad (11)$$

$$Z_f(\omega) = R_1 + [i\omega C_{ad} + (R_2)^{-1} + (R_3 + Z_d)^{-1}]^{-1} \quad (12)$$

Total Electrode Impedance Modeling of HER

It is well known that the faradaic impedance is only a part of the total electrode impedance, so the contribution of the non-faradaic impedance has to be additionally considered, together with the contribution of uncompensated electrolyte resistance.^{31,32} Whereas the uncompensated part of the electrolyte resistance, R_s , originated from the electrolyte solution between the Luggin-end of the reference electrode and the working electrode surface, the origin of the non-faradaic part of the total electrode impedance is related to the charging/discharging of the electrical double-layer of capacitance C_{dl} . In terms of the pure capacitive response of the double-layer charging/discharging, the non-faradaic admittance, $Y_{nf}(\omega)$, is defined as^{31,32}

$$Y_{nf}(\omega) = i\omega C_{dl} \quad (13-a)$$

$$C_{dl} = dq_m / dE \quad (13-b)$$

where q_m denotes the excess charge of the metal.

The double-layer impedance is in the form of the pure capacitive impedance, $(i\omega C_{dl})^{-1}$, situated parallel to Z_f , suggesting no interaction between faradaic and non-faradaic effects.^{31,32} Following the physical electrode configuration during impedance measurements, R_s has to be placed serially with this parallel connection, so the equation for the frequency dependence of the total electrode impedance, $Z_T(\omega)$, can be written in the following form:

$$Z_T(\omega) = R_s + [i\omega C_{dl} + Z_f(\omega)^{-1}]^{-1} \quad (14)$$

Schematic Impedance Spectra of HER

General principles of the impedance spectroscopy used in the kinetic study of HER are visualized in Figures 1 and 2 through schematically presented Bode plots (log of the impedance magnitude, $|Z|$, and phase angle, φ , vs. $\log \omega$). A broad frequency range is covered, $Z_T(\omega)$ is defined by Eq. (14), $Z_f(\omega)$ is defined by Eqs. (11) or (12) and $M(\omega)$ is defined as:

$$M(\omega) = (D/L) (i\omega L^2/D)^{1/2} \coth (i\omega L^2/D)^{1/2} \quad (15)$$

$M(\omega)$ described by Eq. (15) is characteristic of the diffusion of species with diffusion coefficient D within a finite-length region L , and in this case Z_d is defined as^{4,10,26}

$$Z_d = K_\sigma (L/D) (i\omega L^2/D)^{-1/2} \tanh (i\omega L^2/D)^{1/2} = R_d (i\omega L^2/D)^{-1/2} \tanh (i\omega L^2/D)^{1/2} \quad (16)$$

where $K_\sigma (L/D) = R_d$ is a pure resistance term.

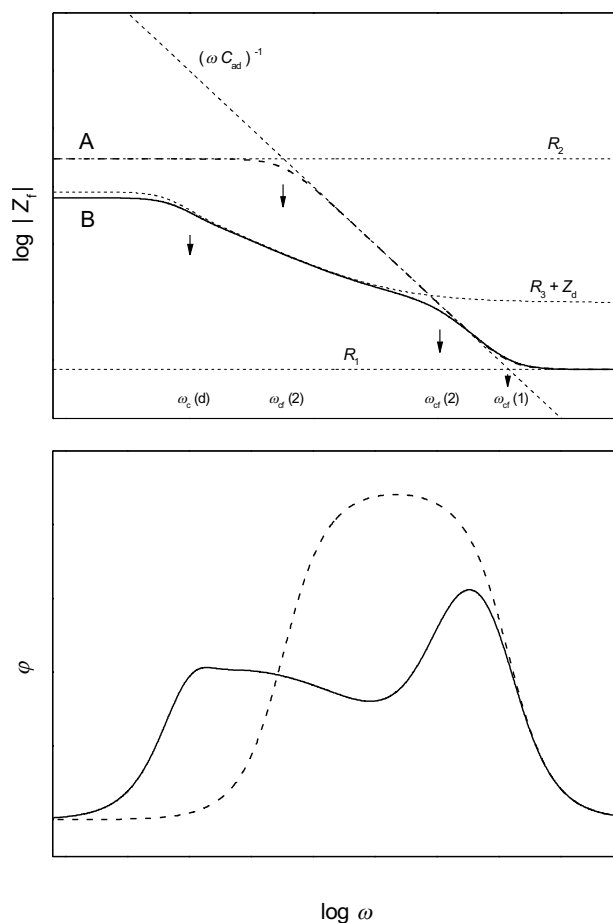


Figure 1. Schematic Bode plot of $Z_f(\omega)$ defined for A (---) Eq. (11), and B (—) Eq. (12) with $M(\omega)$ defined by Eq. (15). Thin dotted lines denote impedances of particular constitutive elements, or their sum. Positions of critical frequencies, $\omega_c(f)$ and $\omega_c(d)$, are denoted by arrows.

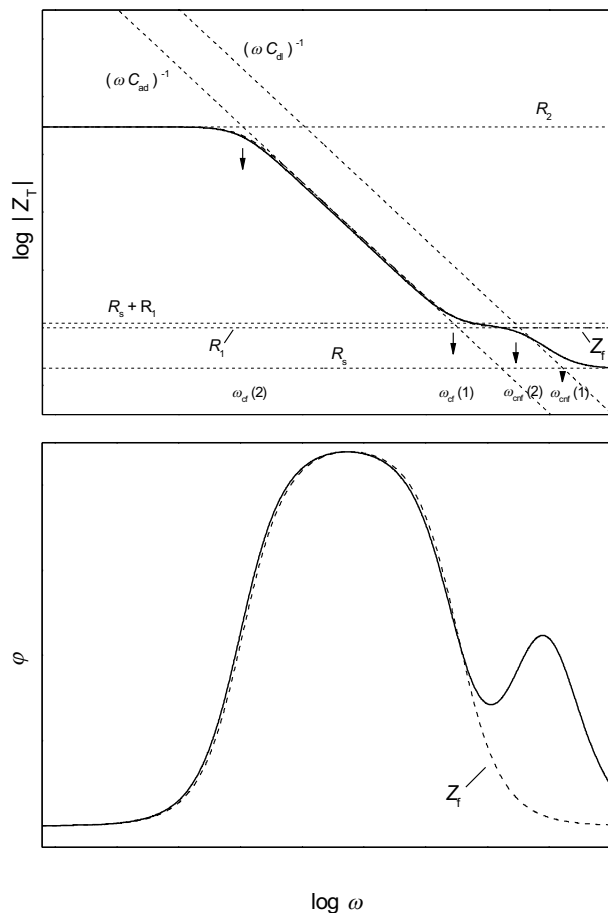


Figure 2. Schematic Bode plot of (—) $Z_T(\omega)$ defined for Eq. (14) with (---) $Z_T(\omega)$ defined by Eq. (11). Thin dotted lines denote impedances of particular constitutive elements, or their sum. Positions of critical frequencies, ω_{cfr} and ω_{cfr} are denoted by arrows.

Schematic Bode plots in Figures 1 and 2 are drawn for an expected order of impedance events.^{31,32} For the faradaic impedance spectrum presented in Figure 1, this means that electron transfer is faster than adsorption, absorption and diffusion, or $R_1 \ll R_2$ and $(R_3 + Z_d)$. At the highest frequencies Z_f tends to R_1 . At the lowest frequencies, Z_f is determined by the lowest impedance in parallel to the capacitive impedance $(i\omega C_{ad})^{-1}$, which are both in accord with the limiting frequency behaviour of Eqs. (11) and (12). Identification of separate impedances is based on their characteristic frequency dependences, as denoted by thin dotted lines in Figures 1 and 2. By simple translations of lines that correspond to impedances of particular elements in Figure 1, it becomes clear how the faradaic impedance spectrum is influenced by the values of particular impedance elements, including limited cases of $R_1 \ll [i\omega C_{ad} + Z_{rest}]^{-1}$ and $R_1 \gg [i\omega C_{ad} + Z_{rest}]^{-1}$. Generally, two faradaic time constants (in the faradaic impedance spectrum seen as two critical angular frequencies $\omega_{cf}(1)$ and $\omega_{cf}(2)$, where there are changes in the slope of $\log |Z|$ vs. $\log \omega$ curves³³ and formation of a maximum in ϕ vs. $\log \omega$ dependencies), are

characteristic of both mechanisms of the faradaic reaction. The first critical frequency, defined as $\omega_{cf}(1) = [C_{ad}R_1]^{-1}$, is equal in two cases, whereas $\omega_{cf}(2)$ is different: $\omega_{cf}(2) = [C_{ad}R_2]^{-1}$ when Z_f is described by Eq. (11), and $\omega_{cf}(2) = [C_{ad}R_2(R_3 + Z_d)(R_2 + R_3 + Z_d)^{-1}]^{-1}$ when Z_f is described by Eq. (12). Note that the multiplier of C_{ad} in this last case is in fact its parallel impedance. As usual, the branch of the lowest impedance determines the impedance of the parallel sum, so various simplified definitions of $\omega_{cf}(2)$ are possible in this case. When diffusion is operative, and $R_2 \gg R_d \gg R_3$ as in Figure 1 B, the mass transfer function, $M(\omega)$, defined by Eq. (15) influences the low frequency part of the impedance spectra, and causes appearance of an additional relaxation frequency, $\omega_c(d) = 2\pi D/L^2$.

Influence of addition of the non-faradaic impedance on the shape of the impedance spectrum is seen in Figure 2. Due to the usual $C_{dl} \ll C_{ad}$, two new critical frequencies appeared due to relaxations of C_{dl} through R_s and $(R_1 + R_s)$. In the scheme in Figure 2, these two criti-

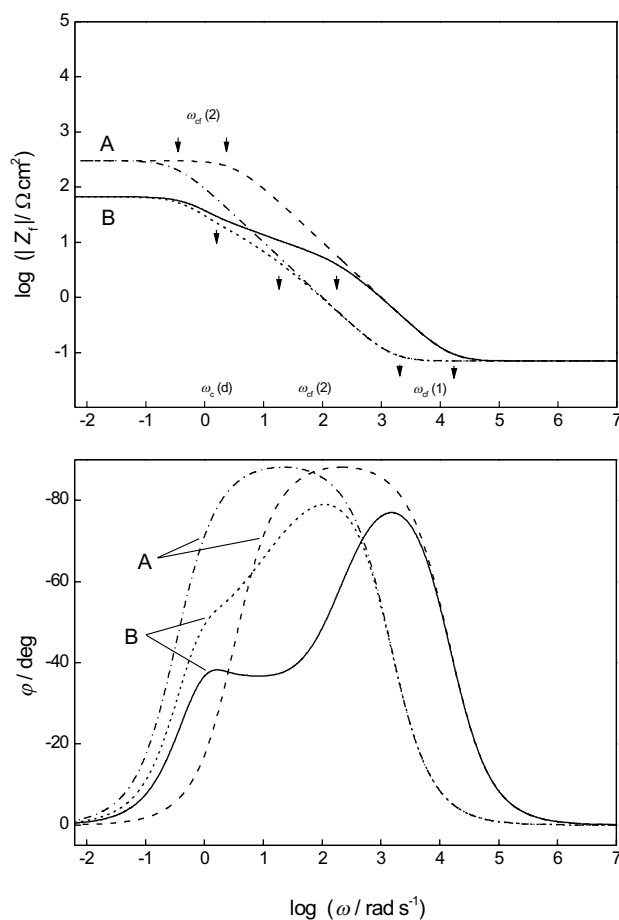


Figure 3. Simulated Bode plots of $Z_T(\omega)$ calculated for A Eq. (11) with $R_1 = 0.07 \Omega \text{ cm}^2$, $R_2 = 300 \Omega \text{ cm}^2$, and B Eq. (12) with $M(\omega)$ defined by Eq. (15), $R_1 = 0.07 \Omega \text{ cm}^2$, $R_2 = 300 \Omega \text{ cm}^2$, $R_3 = 5 \Omega \text{ cm}^2$, $R_d = 80 \Omega \text{ cm}^2$, $L^2/D = 5 \text{ s}$, and the following values of C_{ad} : A (—) and B (---) $1 \times 10^{-3} \text{ F cm}^{-2}$; A (---) and B (----) $1 \times 10^{-2} \text{ F cm}^{-2}$. Positions of critical frequencies, ω_{cf} and $\omega_c(d)$, are denoted by arrows.

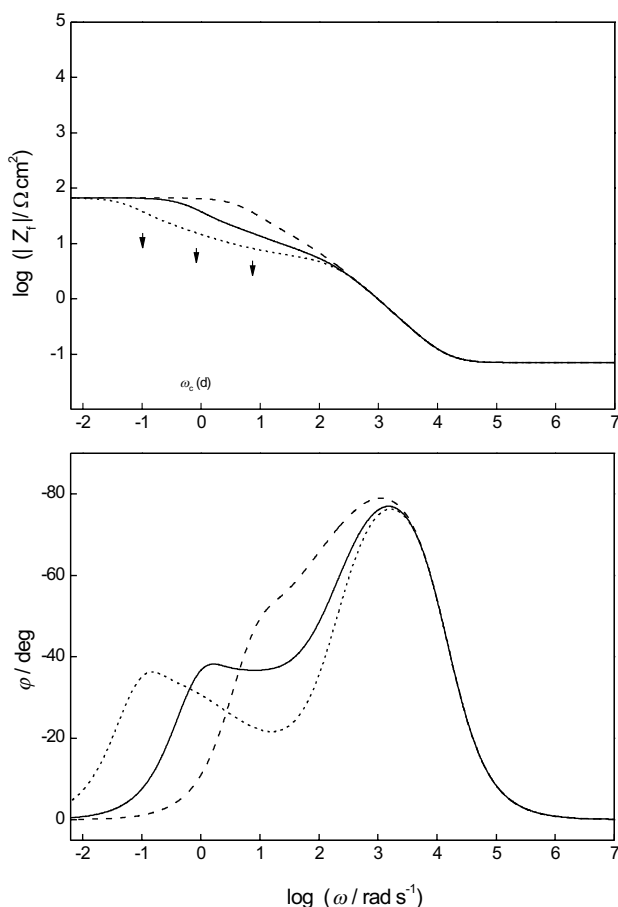


Figure 4. Simulated Bode plots of $Z_f(\omega)$ calculated for Eq. (12) with $M(\omega)$ defined by Eq. (15), $R_1 = 0.07 \Omega \text{ cm}^2$, $C_{ad} = 1 \times 10^{-3} \text{ F cm}^{-2}$, $R_2 = 300 \Omega \text{ cm}^2$, $R_3 = 5 \Omega \text{ cm}^2$, $R_d = 80 \Omega \text{ cm}^2$ and the following values of L^2/D : (---) 0.5 s; (—) 5 s; (····) 50 s. Positions of critical frequencies, $\omega_c(d)$, are denoted by arrows.

cal frequencies are seen at high frequencies as changes in the slope of the $\log |Z|$ curve, or appearance of a maximum in the phase angle curve. New critical frequencies are in Figure 2 denoted as ω_{cnf} and defined as $\omega_{cnf}(1) = (C_{dl}R_s)^{-1}$ and $\omega_{cnf}(2) = [C_{dl}(R_1+R_s)]^{-1}$. If these two ω_{cnf} values are close, such as for $R_1 < R_s$, C_{dl} will not be seen in the impedance spectrum. Here, according to Eq. (14), R_s is in general competition with the impedance $[i\omega C_{dl} + Z_f(\omega)^{-1}]^{-1}$. In the first limiting case of $R_s \ll [i\omega C_{dl} + Z_f(\omega)^{-1}]^{-1}$, only this last impedance will be seen in the spectra, whereas for $R_s \gg [i\omega C_{dl} + Z_f(\omega)^{-1}]^{-1}$, R_s will cover all other impedance events. This can be easily visualized by translations of the R_s -related thin dotted line in Figure 2. Influence of the change in C_{dl} values on the Z_T spectrum can be also seen by translations of $(\omega C_{dl})^{-1}$ thin dotted line. For decreased C_{dl} values, $(\omega C_{dl})^{-1}$ line is shifted toward higher frequencies, resulting in dominance of Z_f over a broader frequency range. For increased C_{dl} values, however, $\omega_{cnf}(1)$ is shifted toward lower frequencies, making double-layer impedance dominant over a broad region of frequencies.

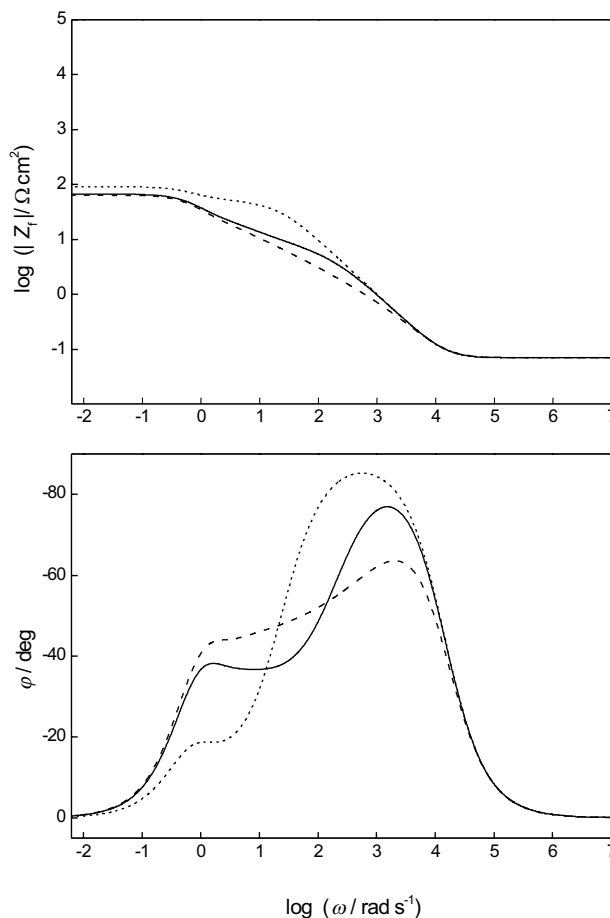


Figure 5. Simulated Bode plots of $Z_f(\omega)$ calculated for Eq. (12) with $M(\omega)$ defined by Eq. (15), $R_1 = 0.07 \Omega \text{ cm}^2$, $C_{ad} = 1 \times 10^{-3} \text{ F cm}^{-2}$, $R_2 = 300 \Omega \text{ cm}^2$, $R_d = 80 \Omega \text{ cm}^2$, $L^2/D = 5 \text{ s}$, and the following values of R_3 : (---) 0.5 $\Omega \text{ cm}^2$; (—) 5 $\Omega \text{ cm}^2$; (····) 50 $\Omega \text{ cm}^2$.

Simulated Faradaic Impedance Spectra of HER

To see practical consequences of changes in the values of particular impedance elements for the shapes of impedance spectra, some simulations were performed using real numerical values of parameters. Thus, simulated Bode plots calculated by the use of Eqs. (11) and (12) are presented in Figure 3 over a broad frequency range, for the expected situation of $R_1 \ll R_2$, an expected value for L^2/D (L is in the range of μm and $D \sim 10^{-9} \text{ cm}^2 \text{ s}^{-1}$), and rather different but already observed^{2,3,5,11-13} values of C_{ad} .

Influence of increased C_{ad} is seen in Figure 3 as a shift of both ω_{cf} toward lower frequencies. Shift of $\omega_{cf}(2)$ toward $\omega_c(d)$ in case B of Figure 3 resulted in decreased resolution between two frequency dependent impedances, $i\omega C_{ad}$ and $(R_3 + Z_d)$. As it is obvious from Figure 4, resolution between two impedance branches becomes more marked as $\omega_c(d)$ is moved toward a lower frequency range. In this context, the low value of the diffusion coefficient is advantageous, since for the constant value of L , a low value of D makes a low $\omega_c(d)$.

For Z_f described by Eq. (12), the part of the spectrum at $\omega < \omega_{cf}$ (2) corresponds to either pure resistance, pure diffusion impedance, or is the sum of both impedances, all in dependence on particular values of R_2 and $(R_3 + Z_d)$. In Figure 5, Bode plots are simulated for increased values of R_3 , showing the screening effect for characteristic frequency dependence of Z_d . The situation can be easily expanded to the case when R_3 dominates over Z_d in the whole frequency range. This case, however, is detrimental, since recognition of the model and resolution between R_2 and R_3 become practically impossible.

Simulated Total Impedance Spectra of HER

According to Eq. (14) with $Z_f(\omega)$ defined by either Eq. (11) or (12), at high frequencies R_s is in competition with $(i\omega C_{dl})^{-1}$ and $Z_f \approx R_1$. Influence of R_1 on the shape of the impedance spectra is presented in Figure 6. Z_T is defined by Eq. (14), Z_f is defined by Eq. (12) and $M(\omega)$ is defined by Eq. (15).

As seen from Figure 6, the influence of increased R_1 values is limited to high-to-medium frequencies, and is

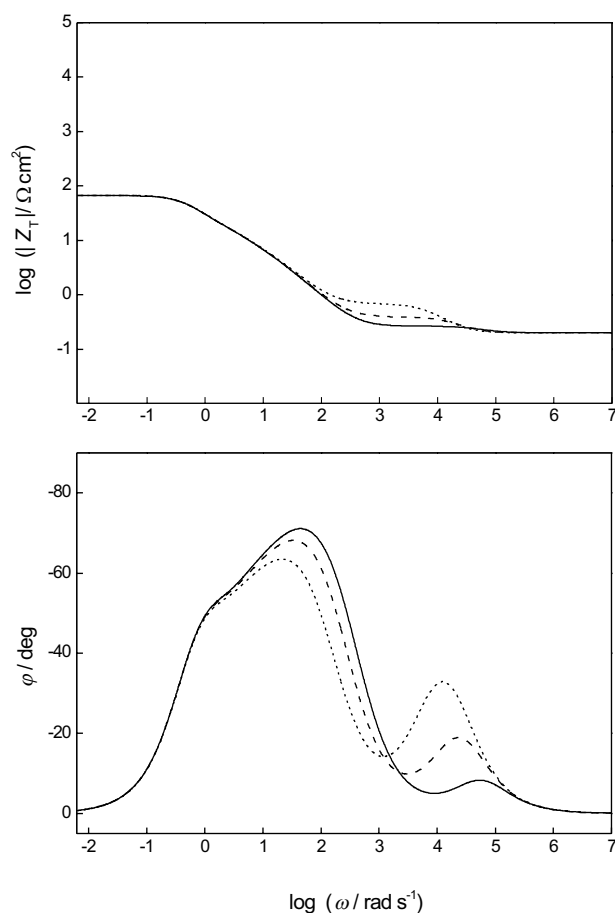


Figure 6. Simulated Bode plots of $Z_T(\omega)$ calculated for Eq. (14), $R_s = 0.2 \Omega \text{ cm}^2$, $C_{dl} = 3 \times 10^{-4} \text{ F cm}^{-2}$, $Z_f(\omega)$ calculated by Eq. (12) with $M(\omega)$ defined by Eq. (15), $C_{od} = 1 \times 10^{-2} \text{ F cm}^{-2}$, $R_2 = 300 \Omega \text{ cm}^2$, $R_3 = 5 \Omega \text{ cm}^2$, $R_d = 80 \Omega \text{ cm}^2$, $L^2/D = 5 \text{ s}$, and the following values of R_1 : (—) $0.07 \Omega \text{ cm}^2$; (---) $0.20 \Omega \text{ cm}^2$; (····) $0.50 \Omega \text{ cm}^2$.

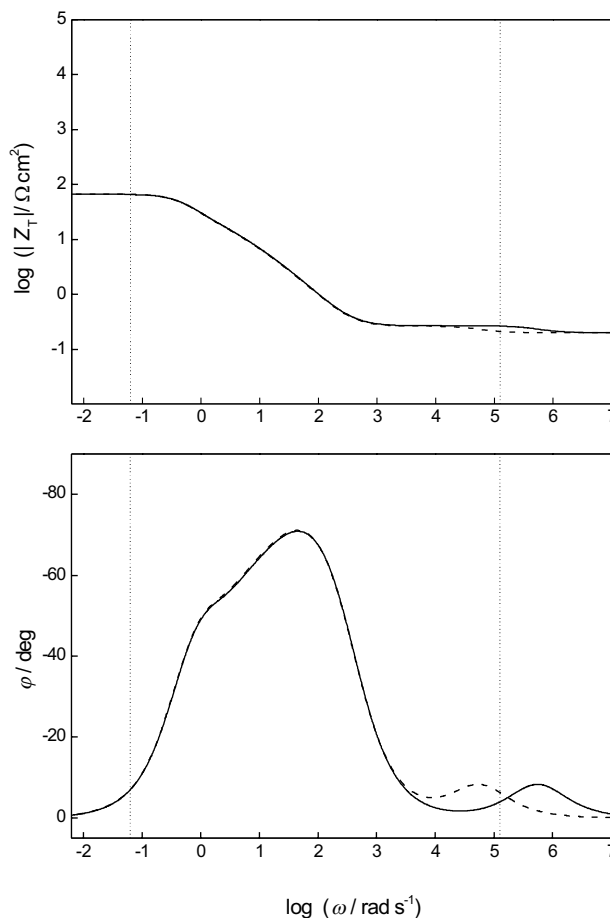


Figure 7. The same as in Figure 6, with $R_1 = 0.07 \Omega \text{ cm}^2$, and the following values of C_{dl} : (—) $3 \times 10^{-5} \text{ F cm}^{-2}$; (---) $3 \times 10^{-4} \text{ F cm}^{-2}$.

manifested in formation of more prominent maxima in phase angle dependences and a better resolution between $(i\omega C_{dl})^{-1}$ and R_1 . In Figure 7, Bode plots are simulated on the basis of Figure 6, and two different C_{dl} values.

As shown from the scheme in Figure 2, in the impedance spectra C_{dl} is clearly seen for $R_1 \gg R_s$. In other words, if $R_1 < R_s$, as for the fast electron transfer reactions, the double layer impedance will hardly be seen in $\log |Z_T|$ vs. $\log \omega$ dependence. Simulations in Figure 7 present such a case, showing the effect of increased C_{dl} as a shift of the maximum of the phase angle curve toward lower frequencies. On the other hand, for a decreased C_{dl} value, the frequency response of the non-faradaic impedance is shifted toward higher frequencies. By limiting the frequency window to the experimentally available range (*cf.* vertical thin lines in Figure 7), it becomes clear how positions of critical relaxation frequencies influence the visible part of the spectra.

There is an additional problem here, related to the non-ideal capacitive response of solid electrodes that originated from the heterogeneity of solid electrode surfaces.^{2,5-7,12,16,19,34} To account for the observed deviations, the constant phase element, CPE, was usually used in-

stead pure capacitance.^{2-5,7,8,10,12,14-16,18-21} Accordingly, Eqs. (11)–(14) should be redefined by changing all $i\omega C$ admittance terms by:³⁴

$$Y_{\text{cpe}}(\omega) = C_{\text{cpe}}(i\omega)^n \quad (17)$$

In Eq. (17) n represents depression of the phase angle *via* $90^\circ(1-n)$, or slope of the capacitive impedance in $\log |Z|$ vs. $\log \omega$ dependence which is different from ideal -1 . Theoretically, n ranges between 1 for ideal capacitive behaviour, and 0.5 for an ideal pore behaviour.³⁵ C_{cpe} is the frequency independent capacity parameter being equal to pure capacitance for $n = 1$.

In Figure 8, Bode plots are simulated by the use of Eq. (14), Z_f is defined by Eq. (11), with both capacitive (C_{dl} and C_{ad}) admittance terms replaced by Eq. (17), and n ranging from 1.00 to 0.50.

Although the main effects of the decrease in n presented in Figure 8 can be described as a decrease of slopes of capacitive impedances, decrease of phase angle maxima, and shifts of both ω_c to higher frequencies,

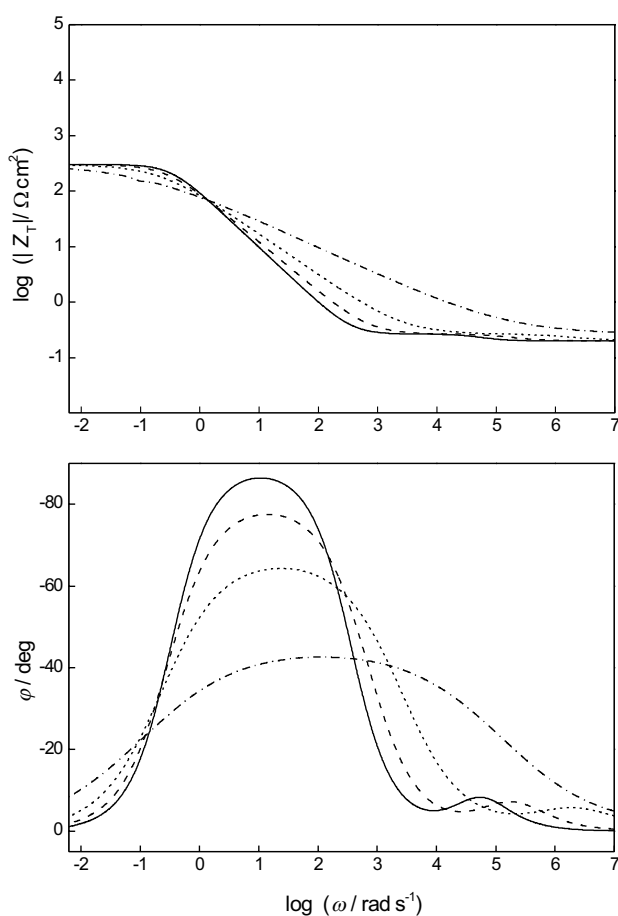


Figure 8. Simulated Bode plots of $Z_T(\omega)$ calculated for Eq. (14) with $Z_f(\omega)$ defined by Eq. (11), all $i\omega C$ terms replaced by Eq. (17), $R_s = 0.2 \Omega \text{ cm}^2$, $(C_{\text{cpe}})_{\text{dl}} = 3 \times 10^{-4} \Omega^{-1} \text{ cm}^{-2} \text{ s}^n$, $R_1 = 0.07 \Omega \text{ cm}^2$, $(C_{\text{cpe}})_{\text{ad}} = 1 \times 10^{-2} \Omega^{-1} \text{ cm}^{-2} \text{ s}^n$, $R_2 = 300 \Omega \text{ cm}^2$, and the following values of n : (—) 1; (---) 0.90; (····) 0.75; (- · - ·) 0.50.

it must be stressed that the decrease of n values changes significantly the shape of impedance spectrum. Thus for $n = 0.50$, the impedance spectrum becomes quite different from its counterpart for $n = 1.00$. In this particular case, differentiation between models for infinite diffusion, CPE, and the infinite porous model is practically impossible. In dependence on surface morphology, but also on the concentration of the electrolyte solution,¹² n ranged between 1.00 and 0.55,^{5,8-10,12,14-16,19,21} which is a considerably broad range of experimentally observed deviations from ideal behaviour. It is our opinion, that n should be kept high, which can be done by using either smooth electrode surfaces or high electrolyte concentrations,¹² since low values of n make the deconvolution procedure very difficult and allow a high extent of possible speculations.

EXPERIMENTAL

Experimental Conditions

Experimental conditions, *e.g.*, the cell (three-electrodes, 0.5 mol dm^{-3} H_2SO_4 , high purity N_2 , 298 K), electrodes (Rh or Ru working, Pt-spiral counter, saturated mercury sulfate reference, Pt-probe pseudo-reference), equipment for impedance measurements (Solartron 1250 FRA & 1286 ECI) and the way of electrode preparation were as described elsewhere.^{21,36} Briefly, working electrodes (0.08 cm^2 of superficial area) were prepared by galvanostatic deposition of either ruthenium or rhodium on the platinum wire. Acid solutions of diammonium hexachloro salts of Rh^{IV} or Ru^{IV} were used, and different deposition times were applied to obtain nearly equal masses of deposited material, as determined by the Cahn C 2000 recording balance equipment. Impedance measurements at each potential value were carried out using the 10 mV amplitude sine-wave signal of frequencies between 20 kHz to 0.01 Hz, and five measured impedance points per decade. Steady-state currents were checked by time-independent currents, and also controlled during impedance measurements when no significant current drifts were observed. All impedance and current values are presented per cm^2 of the superficial electrode surface area, whereas all potentials are quoted with respect to the hydrogen reversible electrode, *rhe*.

Numerical Calculations

Each experimental impedance spectrum was collected in the form of 32 measured data pairs at defined angular frequency, $\omega = 2\pi f$ values. Calculated impedance data were obtained from the corresponding equation(s) for the same ω values. The curve fitting procedure between experimental and calculated data was then performed by the use of the complex non-linear regression algorithm and initial impedance parameter values estimated from experimental impedance spectra at frequencies of their domination. As usual, fit quality plots and average errors of regression³⁰ served as indications for the best-fitted case. The details of the numerical data handling were presented previously.³⁶

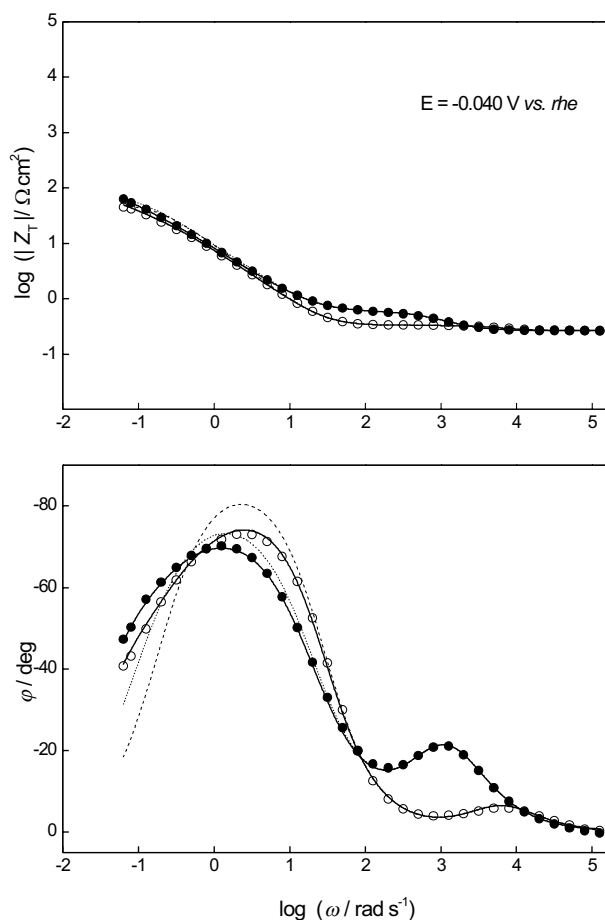


Figure 9. Experimental Bode plots of (●) Ru and (○) Rh electrodes measured in $0.5 \text{ mol dm}^{-3} \text{ H}_2\text{SO}_4$ at $E = -0.040 \text{ V vs. r.h.e.}$. The best fitted plots (—) were calculated by the use of Eq. (14), $Z_f(\omega)$ defined by Eq. (12) with Z_d defined by Eq. (16) and the values of impedance parameters from Table I. Results of the fitting procedure with $Z_f(\omega)$ defined by Eq. (11) are drawn by (---) for the rhodium, and by (-·-·-) for the ruthenium electrode.

RESULTS AND DISCUSSION

Experimental impedance spectra of ruthenium and rhodium electrodes measured at $E = -0.040 \text{ V vs. r.h.e.}$, in $0.5 \text{ mol dm}^{-3} \text{ H}_2\text{SO}_4$ are depicted in Figure 9.

In view of the discussion about the theoretical aspects of impedance spectra of HER, it appears that the measured impedance spectra presented in Figure 9 indicate the presence of a non-faradaic part for both electrodes through the existence of high-frequency maxima in φ vs. $\log \omega$ dependences. No clear prominence of the double-layer capacitance in $\log |Z|$ vs. $\log \omega$ dependence that is obtained particularly for the rhodium electrode can be, according to the scheme in Figure 2 and simulations in Figure 7, explained by the high-frequency faradaic resistance term lower than the electrolyte resistance term. For the ruthenium electrode, the faradaic contribution is clearly evident at $\omega < \omega_{\text{cnf}}$ as the resistive part being followed by a prominent capacitive-like impedance response. For the rhodium electrode, however,

TABLE I. The best fitted impedance parameter values for rhodium and ruthenium/ $0.5 \text{ mol dm}^{-3} \text{ H}_2\text{SO}_4$ electrode impedance spectra presented in Figure 9

	Rh	Ru
$R_s / \Omega \text{ cm}^2$	0.26	0.27
$(C_{\text{dl}})_{\text{cpe}} / \Omega^{-1} \text{ cm}^{-2} \text{ s}^n$	2.3×10^{-3}	5.4×10^{-3}
n_{dl}	0.99	0.95
$R_1 / \Omega \text{ cm}^2$	0.07	0.35
$(C_{\text{ad}})_{\text{cpe}} / \Omega^{-1} \text{ cm}^{-2} \text{ s}^n$	1.0×10^{-1}	1.0×10^{-1}
n_{ad}	0.99	0.92
$R_2 / \Omega \text{ cm}^2$	120	160
$R_3 / \Omega \text{ cm}^2$	~ 3	~ 3
$R_d / \Omega \text{ cm}^2$	220	400
$L^2 (D)^{-1} / \text{s}$	~ 85	~ 85

only capacitive-like impedance is dominant over a broad region of frequencies, suggesting differences in the high frequency faradaic resistance values for the two electrodes. This fact can be supported by the similarity of impedance spectra in Figure 9 and simulations drawn in Figure 6 for increased values of R_1 . The non-blocking behaviour at the lowest frequencies is seen for both electrodes as the presence of resistive-like impedance in parallel with the capacitive impedance. Whether this resistive-like impedance is pure resistance, or finite diffusion impedance is not clear from Figure 9, so fitting procedures were performed using Eq. (14) with $Z_f(\omega)$ defined by either Eq. (11) or (12). All fitting results in Figure 9 are represented by lines, in contrast to experimental results that are represented by marks. As obvious from Figure 9, significant deviations, particularly at low frequencies, are obtained by the use of $Z_f(\omega)$ defined by Eq. (11), whereas the best fitted spectra for both electrodes were obtained for $Z_f(\omega)$ defined by Eq. (12), with Z_d defined by Eq. (16). Values of the corresponding impedance parameters are listed in Table I.

Values of impedance parameters listed in Table I show some differences between the two electrodes. The value of R_1 is about an order of magnitude higher for the ruthenium electrode, indicating slower kinetics of the electron transfer at the constant surface coverage of adsorbed hydrogen. For the ruthenium electrode, the influence of higher R_1 is reflected in higher values of R_2 and R_d , which is in full agreement with kinetic definitions of these parameters.²¹ Also, according to Eq. (10-a), C_{ad} is expected to be lower for higher R_1 , which is also obtained if the influence of the corresponding, lower value of n is taken into account. R_3 values are very low for both electrodes, suggesting near reversible kinetics of the absorption step or a fully diffusion controlled hydrogen insertion, as it was discussed for simulations drawn in Figure 5. Diffusion time constants are equal for the two electrodes, indicating no significant differences in the thickness of two metal layers and diffusion

coefficient values. In view of the discussion for simulations drawn in Figure 4, $\omega_c(d)$ values create conditions for a distinct resolution between $(i\omega C_{ad})^{-1}$ and Z_d impedances for both electrodes. Relatively high C_{dl} values of the few mF cm⁻² for both electrodes indicate rough electrode surfaces with roughness factor ~ 100 , and are similar to that already observed for platinized electrodes.¹² The corresponding values of n indicate a homogeneously distributed double-layer capacitance over the rhodium electrode surface, and a less homogeneously distributed double-layer capacitance over the ruthenium electrode surface. According to simulations depicted in Figure 8, however, both values of n are in the range of values that does not change impedance spectra significantly.

CONCLUSIONS

The impedance spectra of HER at low cathodic overpotentials were analyzed on the basis of the theoretical admittance/frequency function derived previously²¹ for the Volmer-Heyrovsky-Tafel reaction mechanism, involving hydrogen insertion (absorption + diffusion) in parallel to desorption of H₂.

The general shape of the corresponding impedance spectrum was discussed on the basis of schematically constructed impedance spectrum. Influence of each impedance parameter on the shape of the impedance spectrum was followed by simulations of impedance spectra using different numerical values of parameters.

The experimental impedance spectra of rhodium and ruthenium electrodes in 0.5 mol dm⁻³ H₂SO₄ measured -0.040 V *vs.* r.h.e, were found consistent with the derived admittance/frequency function. The impedance parameter values were evaluated by a fitting procedure between theoretical and experimental spectra.

Comparison between the impedance parameter values of HER at rhodium and ruthenium electrodes showed a faster HER and a more homogeneous surface for the rhodium electrode, at low overpotential values at least.

Acknowledgement. – The financial support by the Ministry of Science and Technology of the Republic of Croatia, is gratefully acknowledged.

REFERENCES

1. L. Bai, D. A. Harrington, and B. E. Conway, *Electrochim. Acta* **32** (1987) 1713–1731.
2. A. Lasia and A. Rami, *J. Electroanal. Chem.* **294** (1990) 123–141.
3. X. Y. Choquette, L. Brossard, A. Lasia, and H. Ménard, *J. Electrochem. Soc.* **137** (1990) 1723–1730.
4. P. Ekdunge, K. Jüttner, G. Kreysa, T. Kessler, M. Ebert, and W. J. Lorenz, *J. Electrochem. Soc.* **138** (1991) 2660–2668.
5. L. Chen and A. Lasia, *J. Electrochem. Soc.* **139** (1992) 3214–3219; 3458–3464.
6. P. K. Wrona, A. Lasia, M. Lessard, and H. Ménard, *Electrochim. Acta* **37** (1992) 1283–1294.
7. J. Fournier, P. K. Wrona, A. Lasia, R. Lacasse, J.-M. Lalanette, H. Menard, and L. Brossard, *J. Electrochem. Soc.* **139** (1992) 2372–2378.
8. P. Los and A. Lasia, *J. Electroanal. Chem.* **333** (1992) 115–125.
9. A. K. Cheong, A. Lasia, and J. Lessard, *J. Electrochem. Soc.* **140** (1993) 2721–2725.
10. C. Lim and S.-I. Pyun, *Electrochim. Acta* **38** (1993) 2645–2651.
11. L. Bai, *J. Electroanal. Chem.* **355** (1993) 37–55.
12. L. Bai, L. Gao, and B. E. Conway, *J. Chem. Soc., Faraday Trans.* **89** (1993) 235–242; 243–249.
13. L. Gao and B. E. Conway, *Electrochim. Acta* **39** (1994) 1681–1693.
14. C. Lim and S.-I. Pyun, *Electrochim. Acta* **39** (1994) 363–373.
15. T.-H. Yang and S.-I. Pyun, *J. Electroanal. Chem.* **414** (1996) 127–133.
16. J. Fournier, L. Brossard, J.-Y. Tilquin, R. Côte, J.-P. Dodelet, D. Guay, and H. Ménard, *J. Electrochem. Soc.* **143** (1996) 919–926.
17. T. Zakroczyński, V. Kleshnya, and J. Flis, *J. Electrochem. Soc.* **145** (1998) 1142–1148.
18. J. Barber, S. Morin, and B. E. Conway, *J. Electroanal. Chem.* **446** (1998) 125–138.
19. A. Hitz and A. Lasia, *J. Electroanal. Chem.* **500** (2001) 213–222.
20. A. Króliowski and A. Wiecko, *Electrochim. Acta* **47** (2002) 2065–2069.
21. V. Horvat-Radošević and K. Kvastek, *Electrochim. Acta* **48** (2002) 311–322.
22. D. A. Harrington and B. E. Conway, *Electrochim. Acta* **32** (1987) 1703–1712.
23. J. O'M. Bockris and S. U. M. Khan, *Surface Electrochemistry, a Molecular Level Approach*, Plenum Press, New York, 1993. Ch. 3.
24. P. K. Subramanian, in: J. O. M. Bockris, B. E. Conway, E. Yeager, and R. E. White (Eds.), *Comprehensive Treatise of Electrochemistry*, Vol. 4, Plenum Press, New York, 1981., Ch. 8.
25. B. V. Tilak, C.-P. Chen, and S. K. Rangarajan, *J. Electroanal. Chem.* **324** (1992) 405–414.
26. C. Montella, *J. Electroanal. Chem.* **462** (1999) 73–87.
27. X. Wu, H. Ma, S. Chen, *J. Electrochem. Soc.* **145** (1998) 517–523.
28. C. N. Cao, *Electrochim. Acta* **35** (1990) 831–836; 837–844.
29. B. A. Boukamp, *Equivalent Circuit*, University of Twente, 1989.
30. B. A. Boukamp, *J. Electrochem. Soc.* **142** (1995) 1885–1894.
31. M. Sluyters-Rehbach and J. H. Sluyters, in: E. Yeager, J. O'M. Bockris, B. E. Conway, and S. Sarangapani (Eds.), *Comprehensive Treatise of Electrochemistry*, Vol. 9, Plenum Press, New York, 1984, Ch. 4.
32. C. Gabrielli, *Identification of Electrochemical Process by Frequency Response Analysis*, Solartron Instrument Group, Solartron-Schlumberger, Farnborough, 1984.
33. D. A. Harrington, *J. Electroanal. Chem.* **403** (1996) 11–24.
34. T. Pajkossy, *J. Electroanal. Chem.* **364** (1994) 111–125.
35. R. de Levie, *Electrochim. Acta* **10** (1965) 113–130.
36. K. Kvastek, V. Horvat-Radošević, M. Vuković, and D. Marijan, *J. Electroanal. Chem.* **463** (1999) 29–44.

SAŽETAK

Impedancijski spektri reakcije izdvajanja vodika kod niskih katodnih prenapona

Višnja Horvat-Radošević i Krešimir Kvastek

Impedancijski spektri reakcije izdvajanja vodika pri niskim katodnim prenaponima analizirani su na temelju teorijske funkcije ovisnosti admitancije o frekvenciji, izvedene prvotno za Volmer-Heyrovski-Tafel-ov reakcijski mehanizam uz dodatni stupanj apsorpcije i difuzije vodika. Općeniti principi impedancijske spektroskopije su za ovaj slučaj razloženi uz pomoć shematski konstruiranih impedancijskih spektara. Procjena utjecaja svakoga parametra impedancije na oblik spektra izvedena je pomoću simulacija spektara s različitim vrijednostima impedancijskih parametara. Usporedna mjerenja impedancijskih spektara izvedena su na rutenijevoj i rodijevoj elektrodi pri *rhe*, $-0.040\text{ V vs. }rhe$, u $0.5\text{ mol dm}^{-3}\text{ H}_2\text{SO}_4$. Vrijednosti impedancijskih parametara za rutenijevu i rodijevu elektrodu dobivene su metodom podešavanja teorijskih i eksperimentalno mjerenih spektara. Za obje elektrode je uz prijenos elektrona, adsorpciju vodika i stupanj desorpcije H_2 , kod niskih frekvencija uočen dodatni reakcijski stupanj povezan s apsorpcijom i difuzijom vodika unutar metalnoga sloja. Usporedba veličina impedancijskih parametara dviju elektroda ukazuje na bržu kinetiku reakcije izdvajanja vodika na rodijevoj elektrodi.